The Effect of Carbon Equivalent and Nodularity on Multi-Axial Casting Wall Movement during Spheroidal Graphite Iron Solidification and Cooling

Noah J. Brack, Mingzhi Xu, Jingjing Qing
Georgia Southern University, Statesboro, Georgia, USA

Simon Lekakh
Missouri University of Science and Technology, Rolla, Missouri, USA

ABSTRACT

Spheroidal graphite iron, also known as ductile iron, is an iron-carbon casting alloy used in industry for its good castability, balanced mechanical properties, and low cost. Ductile iron consists of round graphite nodules in an iron matrix. During solidification and cooling, ductile iron castings experience dynamic volume changes due to the precipitation of graphite nodules and formation of austenite. These dynamic volume changes can distort external casting surfaces, causing swell and shrinkage porosity. A novel apparatus was custom built to capture the casting wall movement in real time along three axes. This study found that casting expansion increased with carbon equivalent and decreased with nodularity.

Keywords: ductile iron, casting, swell, wall movement, shrinkage. porosity

INTRODUCTION

Ductile iron is an iron-carbon casting alloy often used to produce castings across several sectors including municipal, waterworks, mining, and automotive. To produce quality castings, the castings must be dimensionally accurate, meet the specified mechanical properties, and be solid or porosity free.[1] Ductile iron differs from gray cast iron because of the round or nodular graphite as opposed to flake graphite.[2] During the solidification and cooling of ductile irons, many complex phase transformations occur between the liquid phase and final microstructure. These phase transformations are greatly influenced by alloy composition. Coupled with external factors such as mold strength, pouring temperature, and riser/gating design, these transformations control mechanical properties, dimensional accuracy, and soundness.

The solidification of ductile iron begins with liquid iron and dissolved carbon. A magnesium addition is made to "spheroidize" the graphite. In hypereutectic compositions, a Carbon Equivalent (CE) greater than 4.3, upon reaching the liquidus temperature, proeutectic graphite nodules begin to form.[3] Upon further cooling to the solidus temperature, austenite dendrites form, and the existing graphite nodules are trapped in the interdendritic spaces.[3,4] One defect seen in ductile iron is commonly referred to as swell or casting wall movement. This happens when there is distortion of external casting surfaces, resulting in poor dimensional accuracy. The outward casting wall movement also makes the formation of shrinkage porosity more severe, due to increased feeding volume.[5,6] Casting wall movement is caused by the formation of a lower density phase, graphite, which increases the overall volume of the solidifying casting.[7] The precipitation of graphite exerts a force on the casting walls. This is known as graphitization pressure. If the strength of the mold walls is insufficient to resist deformation, the walls will move and increase the casting volume.[7] Without sufficient feeding, this additional volume makes it more difficult for graphitization and risering to compensate, resulting in a higher propensity to form shrinkage porosity.[5,7] Currently, such wall movement is difficult to predict in simulation software, due to the lack of experimental data under different processing conditions. A proper understanding of the effects of casting parameters on graphitization pressure and the force applied to mold walls can aid in the development of empirical correlations and more accurate predictive simulation.

It is possible that the nodularity of the graphite could have an effect on the applied pressure due to the differences in growth rate. It is theorized that nodularization of graphite in nodular graphite iron is caused by preferential growth of the graphite normal to the basal plane due to lower interfacial energy.[8,9] The presence of "surface-active elements" such as oxygen and sulfur may cause preferential growth to occur in the prismatic direction according to Skaland.[8] These surface-active elements also provide nucleation points for graphite.[8,10] Growth in the prismatic direction is characteristic of the growth of flake graphite.[8] The growth direction of compacted graphite iron (CGI) is debated, and several theories exist with some theorizing that growth occurs only in the basal direction and others believe it grows in both the prismatic and basal directions.[11] Graphite growth rate is affected by the composition of the iron and cooling rate.[12]

A study by Svidro and Dioszegi, measured the change in wall movement of a cylindrical gray iron sample in the radial and axial directions using the "push rod method" with varying inoculant addition amounts. This method utilizes rods extending from the mold cavity to the outside of the mold and connecting to some form of displacement sensor.[13] As the casting solidifies, the "push rods" will be either pushed or pulled as the casting surface deforms, and displacement from the sensors was recorded. They performed two heats and found a greater expansion on the casting with the larger inoculant addition. The authors theorized that this was due to the distribution of columnar grains forming the casting skin.[13]

Tadesse and Fredriksson studied the effects of carbon content on ductile iron along two axes, using four Linear Variable Differential Transformer (LVDT) sensors.[14,15] The study utilized a silica sand and waterglass mold to measure the changes in a simple plate casting. This study found that with increasing carbon content, casting expansion increased and the formation of microporosity reduced.[14,15] This study also found a difference in expansion between the two horizontal axes likely due to the difference in length of the casting between the two axes. This study did not measure the displacement of the top casting surface due to conflict with pouring location. The authors also theorized that a theoretical limit of carbon content in the ductile iron could optimize graphite growth to minimize the formation of microporosity while still preventing mold wall movement.[14,15] Additionally, this research considers a very rigid mold, unlikely to be utilized in industry.[14,15]

Another study on the expansion of graphite during iron solidification was done by Stefanescu et al. using a chemically bonded sand mold contained in a steel shell to prevent the expansion of the iron due to the collapse of mold.[16] The study found that the casting expansion increased with increasing carbon content, but nodular graphite expanded more than lamellar graphite.[16] A similar study performed by Riposan et al. agreed with Stefanescu's findings that ductile iron expands more than gray iron.[16]

To better understand the casting wall movement during ductile iron solidification, and to develop accurate empirical correlations, more data is required across a wider set of parameters. In addition, casting wall movement of the top casting surface also needs to be determined. This study aims to investigate the effects of carbon equivalent and nodularity on wall movement in ductile iron castings and begin the development of mathematical models for graphitization pressure and wall movement, and to improve the accuracy of shrinkage porosity prediction based on these results.

EXPERIMENTAL METHODS

DESIGN OF NOVEL TESTING APPARATUS

To accurately record wall movement along three axes, a novel testing apparatus was constructed to fixture the casting and properly position the displacement sensors. In order to test a variety of molds, the testing apparatus was designed to be adjustable. The apparatus, shown in Figure 1, consists of a 1/8" thick 48" x 54" steel base plate with welded brackets to hold a ¾"-10 (Unified Coarse) UNC threaded rod anchor. Two horizontally adjustable LVDT stands are magnetically attached to the base plate using four neodymium magnets (Figure 2). The adjustable stands allow the adjustment of the displacement sensors in the vertical direction and the magnetic attachment allows adjustment along the base plane. A vertical mount (Figure 1 supports a displacement sensor above the mold to measure displacement of the top casting surface. Inconel pushrods measuring ½" in diameter with a 1/8" groove, 1/8" from the end of the rod (Figure 3) were placed in the mold in molded holes in each of the three directions. LVDT sensors with an accuracy of ±0.1µm were mounted to each stand and positioned using a laser level to ensure each is colinear with the push rods and 90 degrees apart among three major axes. This allows the recording of displacement along three directions arranged in a triad. Calibration of the LVDT sensors was performed using a factory calibrated Computer Numerical Control (CNC) mill, and three separate trials with smaller rectangular castings were performed to ensure the sensors read consistently. Local cooling curves were also recorded using K-type thermocouples. All data acquisition was done with an 8-channel data acquisition unit at a sample rate of 1 Hz. More details on thermocouple location can be found in the section, *Heat Procedure*.

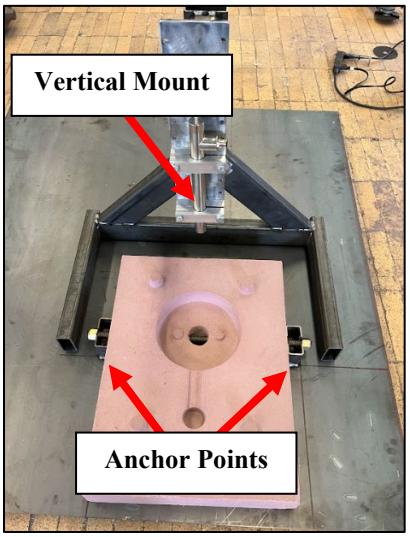

Figure 1. Vertical LVDT mount and baseplate with drag mold half and fixture rod in place.

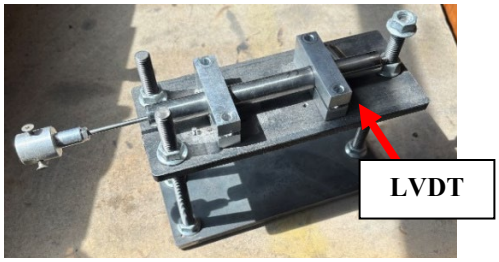

Figure 2. Horizontal LVDT base with LVDT sensor mounted.

Figure 3. Inconel push rods with machined grooves to ensure connection between casting and pushrods.

SAMPLE DESIGN AND MOLD PREPERATION

A drafted cylindrical geometry measuring 8 inches in diameter and 4 inches tall was designed as the testing geometry as shown in Figures 4 and 5. The sample has a boss on the bottom surface, so when the casting solidifies it will be anchored to a threaded rod. The casting is fed by a single in-gate measuring 1.5”x 0.5.” A 3D printed match plate pattern (Figure 6) was built and guide holes for push rods were drilled in the flask. Sand molds were prepared using a nobake sand mixer. An ester-set polyurethane resin was used at 1.2% resin, 35% of 1.2% co-reactant. The Inconel push rods were inserted into the flask with 1” protruding and were molded around. Mold halves were produced one at a time and allowed to set for 48 hours to ensure consistent mold strength across all three heats.

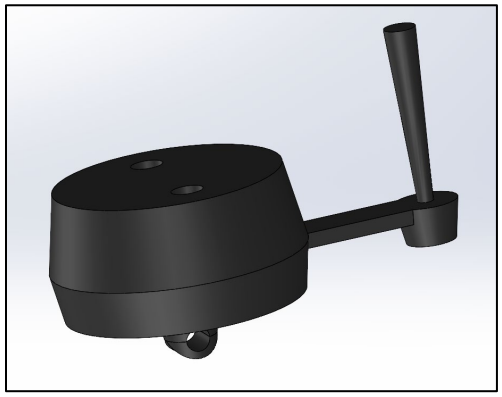

Figure 4. Three-dimensional model of the sample casting with anchoring point at the bottom, gating system is also shown.

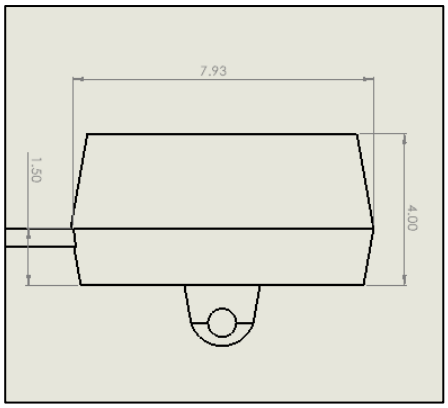

Figure 5. Sample geometry dimensions from the side view, units are in inches.

Figure 6. Drag pattern with fixture rod inserted prior to molding.

SELECTED PARAMETERS

Carbon equivalent and nodularity were selected as the first parameters to study due to the hypothesized large effects of graphite formation on casting wall movement. Three heats were performed. The composition of each heat is shown in Table 1. Heat 1 is a low nodularity hypereutectic iron. Heat 2 is a high nodularity hypoeutectic iron. Heat 3 has similar composition to Heat 1, but with a higher nodularity. Collection of a chilled

sample was unsuccessful for heat 3 so expected chemistry is shown and denoted by an asterisk.

Table 1. Selected Chemistry for Heats 1-3 *Expected Value

Heat #	Element Wt.%							CE (%)
	C	Si	Mg	S	Mn	P	Cu	
1	3.68	2.88	0.038	0.011	0.64	0.006	0.094	4.6
2	2.66	2.48	0.050	0.010	0.44	0.022	0.060	3.5
3	3.71	3.03*	0.055*	0.010	0.44*	0.022*	0.065*	4.7*

HEAT PROCEDURE

For each heat, holes were drilled for thermocouple quartz sleeves ½" to the left of each push rod as shown in Figure 7 and blown out using compressed air. Thermocouple sleeves were then inserted and glued in place using an acetone-based mold glue. Inconel pushrods were inserted into the mold ½" from the wall of the mold cavity. The rods were marked at the appropriate length and removed. The mold was then assembled and glued together with an acetone-based glue. The push rods were then reinserted into the mold and the LVDT's were connected to the back of the push rods. A laser level was then used to align the sensors with the pushrods. Weights (of the same mass) and a pouring basin were placed on top of the mold as shown in Figure 8. K-type thermocouples were placed into the quartz sleeves and all sensors were connected to the data acquisition system.

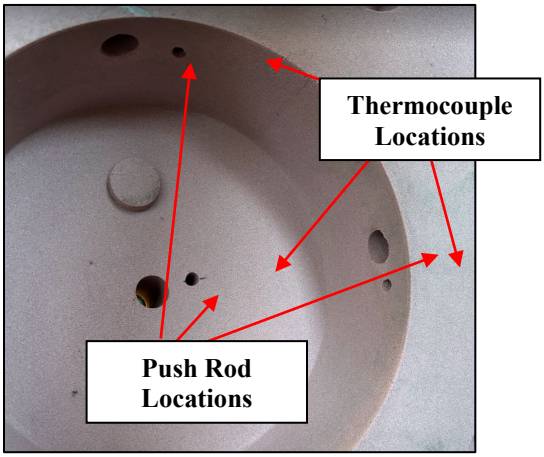

Figure 7. Thermocouple locations placed ½" away from push rod locations.

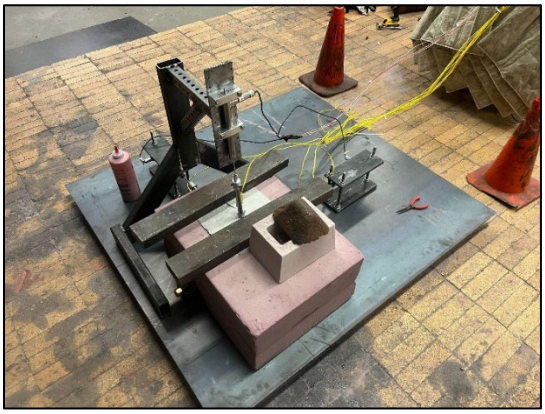

Figure 8. Instrumented mold prepared with all sensors connected, prior to the installation of sensor shielding.

The iron was melted in a 100 lb. induction furnace. The charges consisted of pig iron, ferritic ductile iron returns, steel, and alloy additions. Each melt was tapped at 1480C (2696F). A calcium and cerium containing Fe-Si inoculant was added into the ladle prior to the pour at a 0.15 wt.% addition rate. A 5wt.% Mg nodulizer was used with a sheet steel cover. The chemical compositions for the inoculant and nodulizer are shown in Table 2. Prior to tapping, thermal analysis cups were poured. Chemistry samples were poured in a chill mold. The mold was poured and allowed to cool to room temperature before shakeout.

Table 2. Chemical Composition of Inoculant and Nodulizer

Wt. %	Si	Ca	Ce	Al	Mg	RE
Inoculant	73.09	0.96	1.84	0.97	-	not provided
Nodulizer	45.99	0.80	-	0.46	5.71	0.01

DATA ANALYSIS

Displacement and temperature data was recorded from the time of pouring casting to when the casting cools to below 700C (1292F). The data was processed using MATLAB. The voltage output of the LVDT sensors was converted to displacement using the conversions from calibration on the CNC mill. The casting was 3D scanned using a laser 3D scanner for overall geometry inspection. The 3D scans of the sample castings were compared to the CAD model to determine surface distortion. Chemistry analysis was completed using a Carbon-Sulfur combustion analyzer and an optical emission spectrometer. Metallography samples were polished to a 0.1 µm finish using standard metallographic practices and analyzed with an optical microscope to determine nodularity according to the American Foundry Society (AFS) ductile iron microstructure rating chart. Nodule count was determined using image analysis with ImageJ. Etched micrographs were etched with 5% Nital.

RESULTS

All heats had displacement, cooling curves, thermal analysis, chemistry, and 3D scan data collected.

METALLOGRAPHY

Micrographs were t[200 µm]for nodularity and microst[200 µm]e analysis. Samples were taken from the ingate of each casting as shown in Figure 9. Unetched and etched microstructure of heat 1 is shown in Figure 10 (a) and (b) respectively, unetched and etched microstructure of heat 2 is shown in Figure 11 (a) and (b) respectively, unetched and etched microstructure of heat 3 is shown in Figure 12 (a) and (b) respectively. Nodularity of all samples were summarized into Table 3.

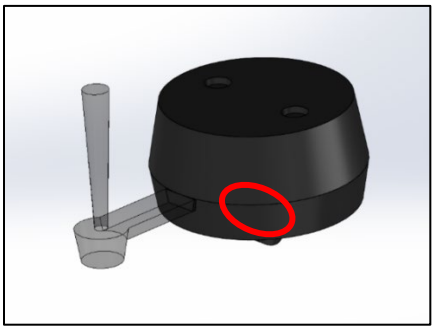

Figure 9. Metallography sample location: casting ingate.

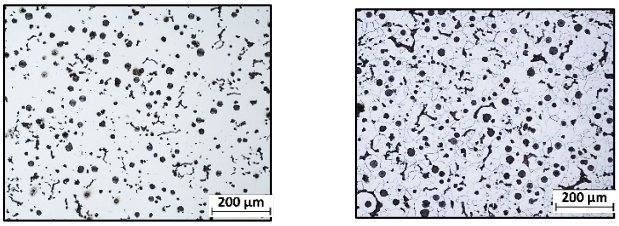

(a) (b)

Figure 10. Heat 1 unetched (a) and etched (b) micrographs.

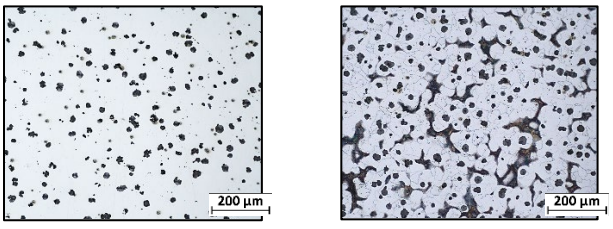

(a) (b)

Figure 11. Heat 2 unetched (a) and etched (b) micrographs.

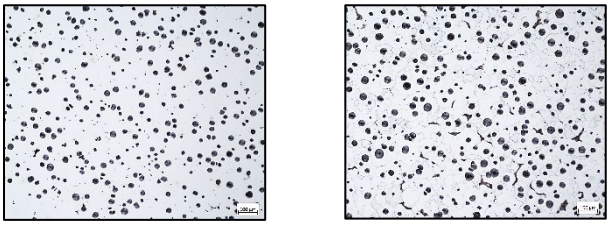

(a) (b)

Figure 12. Heat 3 unetched (a) and etched (b) micrographs.

Table 3. Nodularity and Nodule Count Results of Heats 1-3

Heat #	Nodularity (%)	Nodule Count (#/mm^2)
1	60	355.7
2	90	236.1
3	95	408.3

THERMAL ANALYSIS

Thermal analysis was performed, and the key parameters are listed in Table 4. In specific, *TL* denotes the liquidus temperature. The thermal analysis cups were poured at too low temperature so the liquidus temperatures were not captured correctly. *TE Low* denotes the lowest eutectic temperature. *TE High* denotes the highest eutectic temperature. *R* denotes recalescence, or the difference between TE High and TE Low. *TS* denotes the solidus temperature.

Graphite formation (GRF) numbers are calculated parameters from the thermal analysis system. *GRF 1* is a parameter indicative of the amount of graphite precipitated between TE High and TS. High GRF 1 numbers indicate more eutectic graphite formation. *GRF 2* indicates the thermal conductivity of the iron near solidus and can be used to predict the shape of graphite. Higher GRF 2 numbers indicate lower thermal conductivity and less graphite formation.

Table 4. Thermal Analysis Results

	Heat 1	**Heat 2**	**Heat 3**
TL	-	-	-
TE Low	1145.0	1138.7	1150.5
R	3.7	1.5	2.4
TE High	1148.7	1140.2	1152.9
GRF 1	84	70	94
GRF 2	91	137	91
TS	1094.6	1096.7	1103.4

DISPLACEMENT DATA

Displacement data was processed and plotted using MATLAB. Displacement curves are solid lines and cooling curves are dashed. Top, front, and side directions are denoted in Figure 13. Figures 14-16 show the

displacement and temperature vs. time of heats 1-3, respectively. The novel testing apparatus was successful in capturing displacement of mold walls along three axes. Significant differences in displacement were recorded between heats. The largest expansion recorded was a 2.8 mm expansion in the vertical axis of heat 1. The greatest contraction seen was a 2.7 mm contraction (-2.7 mm displacement) in the vertical axis of heat 2. The horizontal axes produced similar displacements in each heat. Both axes were theorized to have similar displacement results, however, in this study, the front measurement consistently recorded an expansion, and the side measurement consistently recorded a contraction.

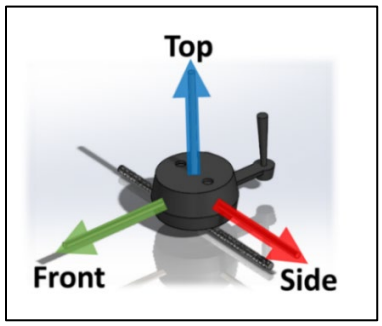

Figure 13. Displacement directions are defined as shown in plotted data.

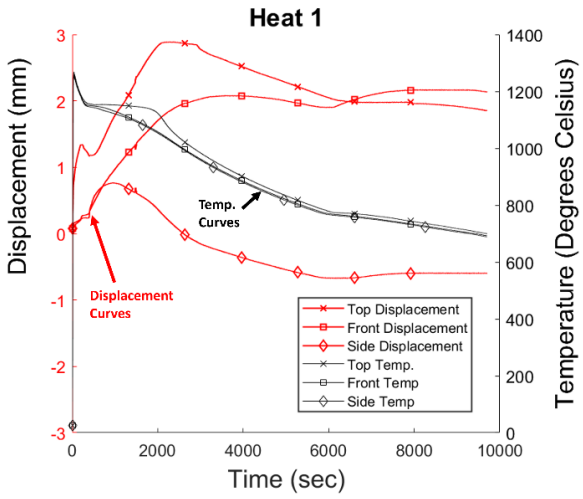

Figure 14. Heat 1 displacement and temperature vs. time.

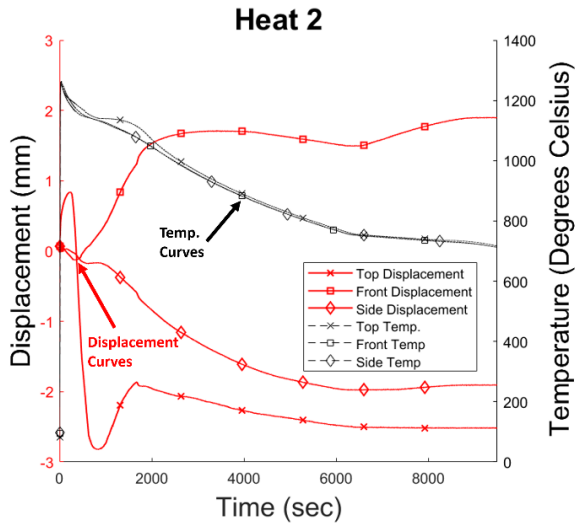

Figure 15. Heat 2 displacement and temperature vs. time.

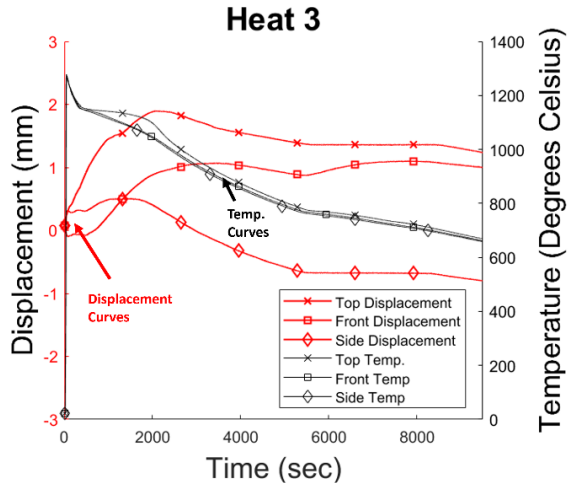

Figure 16. Heat 2 displacement and temperature vs. time.

3D SCAN ANALYSIS

3D scans of the cooled castings were taken and the generated STL files were analyzed for top casting surface distortion. The files were imported into a mesh editor and subjected to a horizontal light source from the right side of the image. A top view shows the location of shadows and therefore lower points on the top surface. The results are shown in Figures 17-19.

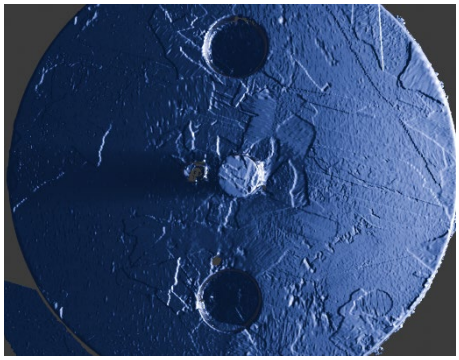

Figure 17. Heat 1 top surface scan images processed in blender with a horizontal light source.

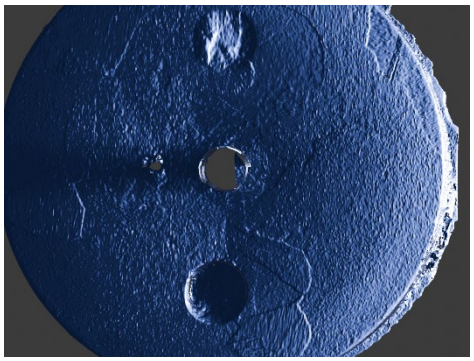

Figure 18. Heat 2 top surface scan images processed in blender with a horizontal light source.

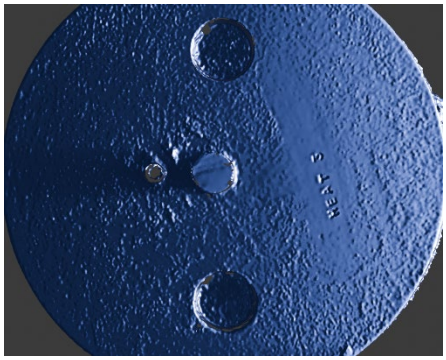

Figure 19. Heat 3 top surface scan images processed in blender with a horizontal light source.

DISCUSSION

CURVE ANALYSIS

As the casting solidified, displacement changed significantly with transformations occurring. As shown in Figure 20, some initial expansion is seen in the vertical axis. This is likely due to the movement of liquid iron upwards as it fills the mold cavity. The rod then sinks back down into the liquid. As the skin forms and is able to support the pushrod, expansion begins and continues until the eutectic transformation. Heat 2 shows a similar trend but contracts significantly following the initial flotation. All horizontal measurements show similar trends across all three heats. A consistent expansion until the eutectic transformation in the front direction and an expansion followed by a steady contraction in the side direction. The difference behavior (expansion vs contraction) along the front and side directions could be a result of interference with gating system, but this needs to be validated through further simulation work.

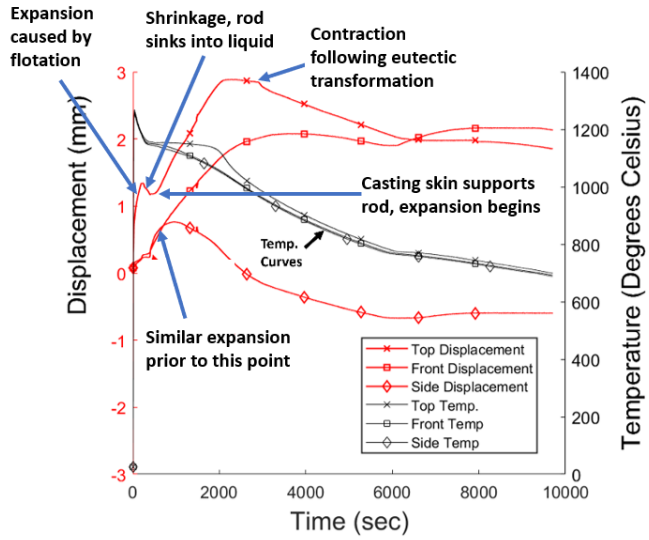

Figure 20. Displacement vs. time of heat 1 annotated.

CE EFFECT

It was observed that CE had a significant effect on the displacement results. Both high CE heats (Heats 1 and 3) showed expansion on the vertical axes (+2.8 mm and +1.9 mm) whereas the low CE heat (Heat 2) showed an initial expansion of 0.9 mm and then contracted to -2.9 mm. This is likely related to the amount of graphite formation as reflected in the thermal analysis.

When comparing the GRF numbers among three heats as shown in Table 4, the greater formation of eutectic graphite (reflected in the higher GRF1 numbers) seen in heats 1 and 3 (both hypereutectic compositions) are theorized to cause greater expansion by applying pressure to the “mushy” iron as the casting skin is formed. The continued formation of graphite prevents significant shrinkage of the casting wall as the liquid transforms into austenite. In heat 2, (a hypoeutectic composition) less eutectic graphite is formed (reflected in the lower GRF1 number), less total graphite is formed (shown by higher GRF 2), and austenite dendrites form as the primary phase. This causes the contraction seen in heat 2. During the secondary formation of graphite, the existence of the austenite dendrite network and further skin solidification resists the pressure applied from graphite formation to a greater extent.

NODULARITY EFFECT

Heats 1 and 3 had similar CE but low (~60%) nodularity and high (~95%) nodularity, respectively. Both heats showed similar trends with the vertical and front measurements expanding and the side contracting. The low nodularity heat 1, however, expands more and reaches a maximum of +2.8mm on the vertical axis. The high nodularity heat reached only +1.8mm of expansion and lacked the brief contraction seen in heat 1.

It is possible that the graphite growth occurring faster in vermicular graphite vs. nodular graphite could cause the increased expansion seen in Heat 1. It is worth noting that from previous research[16,17] ductile iron had a greater initial expansion compared to gray iron, which explains the general expectations of more shrinkage porosity in ductile iron vs. gray iron. Results from heats 1 and 3 had suggested a lower nodularity in ductile iron can further increase the initial expansion, making the shrinkage porosity more severe.

3D SCAN COMPARISON

To further verify the contraction and expansion results recorded via displacement measurements during casting, views of the 3D scanned top surface were rendered. The concavity or convexity of the top surface can be displayed by analyzing the shadowed regions. The top surfaces of the castings from heats 1 and 3 display a convex shape with no shadows on the side facing the light source.

Both heats 1 and 3 also displayed an expansion in the vertical direction (+2.8mm and +1.9mm respectively). The top surface of heat 2 has a concave shape. The presence of the center shadowed region on the side facing the light source highlights the lowered region in the center of the casting. The highlighted regions are displayed in Figures 21-23. These results further indicate that casting dimension accuracy is heavily affected by the graphitization during solidification.

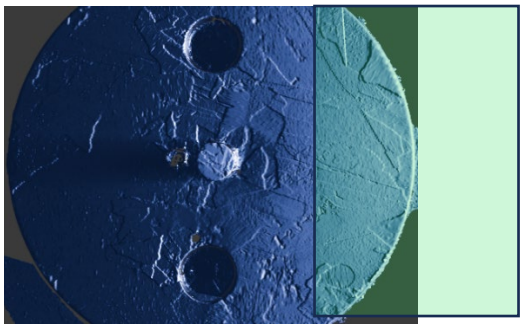

Figure 21. Heat 1 top casting surface with no-shadow region highlighted in green.

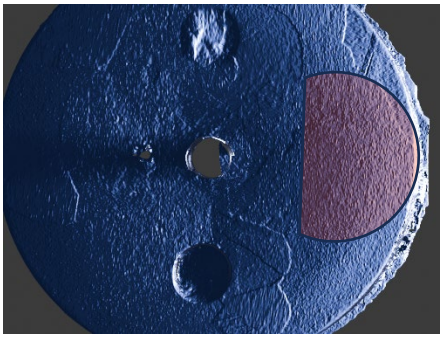

Figure 22. Heat 2 top casting surface with no-shadow region highlighted in green.

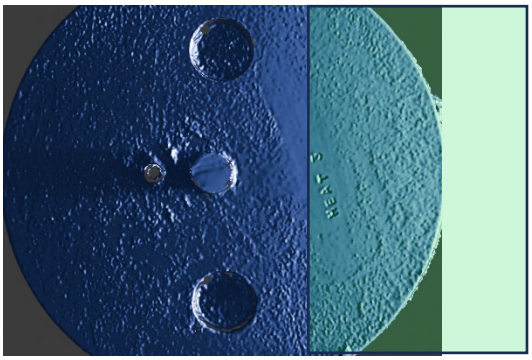

Figure 23. Heat 3 top casting surface with no-shadow region highlighted in green.

FUTURE WORK

Internal porosity distributions of these castings will be analyzed. To further verify the effects of CE and nodularity, heats of intermediate values of CE and nodularity could be performed. To prevent porosity formation in castings via graphite growth, higher CE ductile iron shows greater expansion and greater capability to combat liquid contraction. To prevent swell-related defects, ensure mold strength is sufficient to resist deformation from graphitization pressure. It is important to remember that this study only investigated these effects in rigid nobake sand molds. Future studies would do well to investigate these effects in weaker green sand molds, as well as in even more rigid molds.

CONCLUSION

Using the testing apparatus, displacement was successfully measured across three separate heats. These heats investigated the effects of CE and nodularity on wall movement in ductile iron castings. Significant differences in wall movement were seen between heats and show the effects that metallurgical changes can have on the dimensional changes of the casting during solidification and cooling. Low nodularity, high CE showed the greatest expansion at +2.8mm in the vertical direction. High nodularity, low CE showed the greatest contraction at -2.7mm. The horizontal displacement

measurements showed less correlation to CE and nodularity and showed similar trends across all heats. Additional research and data are required prior to the creation of mathematical models for the prediction of wall movement via simulation. This research provides a template for the continued study of these phenomena and expansion of the parameter set in order to create a more complete model.

ACKNOWLEDGEMENTS

This study was completed as a part of an American Foundry Society funded project (AFS) (21-22#03). This project was also funded by the National Science Foundation (award #2347391). The guidance and materials donation of the project's steering committee are greatly appreciated. All members of the Georgia Southern foundry research team who assisted in experimental setup are appreciated as well.

REFERENCES

1. Dutile Iron Marketing Group, " Designing with Ductile Iron to Achieve Strength and Economy," *Engineered Casting Solutions Vol. 1,* pp. 47-50 (1999).
2. Donoho, C.K., "Ductile Iron Graphite Form Classification," *AFS Transactions* pp. 297-303 (1961).
3. Qing, J., Richards, V.L. and Van, D.C., "Examination of Nodular Graphite Formation and Austenite Solidification in Ductile Iron," *119th Metalcasting Congress, AFS Transactions*, 123, pp.271–281 (2015).
4. Viswanathan, S., Samuel, C., "Solidification of Ductile Iron Revisited," *AFS Transactions*, pp. 431-439 (2011).
5. Ecob, Chris, "A Review of Common Metallurgical Defects in Ductile Cast Iron Causes and Cures," Elkem Foundry Products Division, Oslo, Norway (2005).
6. Dwyer, Z.B., Griffin, R.D., Bates, C.E., "Defects in Ductile Iron Castings," *AFS Transactions,* pp. 89-95 (1996).
7. Torellio, L.I., Wallace, J.F., "Mold Cavity Enlargement in Gray Iron Castings as Controlled by Green Sand Mold Additives," *AFS Transactions*, pp. 404-417 (1963).
8. Skaland, T., Grong, Ø. & Grong, T., "A Model for the Graphite Formation in Ductile Cast Iron: Part I. Inoculation Mechanisms," *Metal Trans A,* **24**, 2321–2345 (Oct. 1993). https://doi.org/10.1007/BF02648605 (Link last accessed 2-5-2025.)
9. Loper Jr., C.R., Fang, K., "Structure of Spheroidal Graphite in Cast Iron," *AFS Transactions* pp. 673-682 (2008).
10. Sommerfeld, A., Tonn, B., "Theory of Graphite Nucleation in Lamellar Graphite Cast Iron," *International Journal of Metal Casting,* Vol. 3, Issue 4 (2009) pp. 39-47.
11. Alonso, G., Stefanescu, D.M., Larranaga, P., Suarez, R., "Graphite Nucleation in Compacted Graphite Cast Iron," *International Journal of Metalcasting* (March 2020). (Link last accessed 2-5-2025.)
12. Brown, B.F., Hawkes, M.F., "Kinetics of Graphitization in Cast Iron," *AFS Transactions,* pp. 181-198 (1951).
13. P. Svidró & A. Diószegi, "On problems of volume change measurements in lamellar cast iron," *International Journal of Cast Metals Research*, 27:1, 26-37 (2014). DOI:10.1179/1743133613Y.0000000075 (Link last accessed 2-5-2025.)
14. Abel Tadesse & Hasse Fredriksson, (2017) "Volume change during the solidification of grey cast iron: its relation with the microstructural variation, comparison between experimental and theoretical analysis," *International Journal of Cast Metals Research*, 30:3, 159-170 (2017). doi: 10.1080/13640461.2016.1277851(Link last accessed 2-5-2025.)
15. Tadesse, A. and Fredriksson, H. (2018) 'The effects of carbon on the solidification of nodular cast iron-its study with the help of linear variable differential transformer and microstructural analysis', International Journal of Cast Metals Research, 31(2), pp. 108–117 (2018). doi:10.1080/13640461.2017.1377382 (Link last accessed 2-5-2025.)
16. Alonso, G., Stefanescu, D.M., Suarez, R., Loizaga, A., Zarrabeita, G., "Kinetics of Graphite Expansion During the Solidification of Lamellar and Spheroidal Graphite Iron," *AFS Transactions,* pp. 237-248 (2014).
17. Riposan, I., Stan, S., Chisamera, M., Neacsu, L., Cojocaru, A.M., Stefan, E., Stan, I., "Simultaneous thermal and contraction/expansion curves analysis for solidification control of cast irons," *China Foundry*, Vol. 17, pp. 96-110 (2020). https://doi.org/10.1007/s41230-020-9147-x (Link last accessed 2-5-2025.)